Gyrokinetic particle simulation of a field reversed configuration

D. P. Fulton,[1,a)] C. K. Lau,[1] I. Holod,[1] Z. Lin,[1,b)] and S. Dettrick[2]
[1]*Department of Physics and Astronomy, University of California, Irvine, California 92697, USA*
[2]*Tri Alpha Energy, Inc., Rancho Santa Margarita, California 92688, USA*

Gyrokinetic particle simulation of the field-reversed configuration (FRC) has been developed using the gyrokinetic toroidal code (GTC). The magnetohydrodynamic equilibrium is mapped from cylindrical coordinates to Boozer coordinates for the FRC core and scrape-off layer (SOL), respectively. A field-aligned mesh is constructed for solving self-consistent electric fields using a semi-spectral solver in a partial torus FRC geometry. This new simulation capability has been successfully verified and driftwave instability in the FRC has been studied using the gyrokinetic simulation for the first time. Initial GTC simulations find that in the FRC core, the ion-scale driftwave is stabilized by the large ion gyroradius. In the SOL, the driftwave is unstable on both ion and electron scales. © 2016 AIP Publishing LLC. [http://dx.doi.org/10.1063/1.4930289]

I. INTRODUCTION

A field-reversed configuration (FRC) is an elongated prolate compact toroid formed without toroidal magnetic field.[1] FRCs were accidentally discovered in the late 1950s upon the application of a reversed-direction bias magnetic fields to theta pinches.[2,3] They were not studied intensively until two decades later, when they were recognized to have several properties favorable for fusion reactors. The FRC represents a high β plasma with surprisingly good macroscopic stability. The compact nature of the plasma and lack of toroidal magnetic field simplify many engineering requirements of a fusion reactor. Engineering is also aided by the scrape-off-layer (SOL), which encloses the plasma core and extends to the device ends, acting as a natural divertor. The high β, high temperature, low collisionality plasma of laboratory FRCs is also characteristic of a number of space and astrophysical plasmas, including those in the outer solar corona, solar superflares,[4] and in accretion discs.[5] A resurgence of interest in FRCs since the late 1980s has contributed to both theoretical and experimental advances in FRC physics in the last 25 years.[6]

It was suggested by Rostoker *et al.*, in 1993, that adding a significant energetic ion population via neutral beam injection (NBI) would improve FRC macro-stability but, due to the large ratio of the fast ion Larmor radius to the plasma size, would not significantly contribute to the destabilization of micro-turbulence, thus preserving the FRCs favorable transport properties.[7–12] In 2008, Tri Alpha Energy, Inc. (TAE) launched a campaign on the FRC experiment, C-2, a facility designed to demonstrate the viability of the NBI conjecture as a step towards an aneutronic fusion reactor concept.[13] Goals of this campaign included understanding fast particle effects on stability and transport in an FRC, developing tightly coupled simulation and theory capabilities, and building global collaborations to achieve these ends. To date, the C-2 campaign has succeeded in demonstrating significantly longer and reproducible confinement using NBI.[14–16] Analysis of data from over 40 000 C-2 discharges is ongoing with great need for simulation and theoretical analysis to rigorously understand transport scaling.

Historically, short confinement times in FRCs have limited thorough studies of transport, however, much work has been done to identify contributing physics. Particle,[17,18] flux,[19] and energy confinement are well identified as anomalous. Possible electrostatic micro-instabilities have been investigated,[20] with the lower hybrid drift instability (LHDI) identified as the most linearly unstable. Numerical simulations of the linear LHDI have been carried out,[21–23] however nonlinear transport and saturation mechanisms have not been investigated. Electron-temperature-gradient-driven electromagnetic modes may also be present in FRCs (Refs. 24 and 25) but have not been studied in detail. The perturbed magnetic field associated with these electromagnetic instabilities can disrupt flux tubes thus contributing to anomalous resistivity.[26] In general, electromagnetic effects may be important to drift instabilities due to the high-β characteristic of FRC plasmas.[27] The plasma edge, near the separatrix, is of particular interest in understanding confinement properties. Confinement is significantly affected by radial diffusion through the edge,[28,29] where particles may move from the closed field lines of the core to the open field lines of the SOL. A number of analytical studies have been made of classical transport in simple equilibria[30–33] and using quasi-steady 1-D plasma profiles.[34–36] Numerical models of transport have included more details using both simple 1-D and 2-D equilibria.[17,19,37–40]

A thorough, theoretical understanding of FRC transport scaling is critical to predict confinement properties as experiments move towards fusion relevant densities and temperatures. To our knowledge, first-principles simulation of turbulent transport in a realistic FRC geometry has not been previously carried out. To investigate the FRC transport, we

---

a)Author to whom correspondence should be addressed. Electronic mail: dfulton@uci.edu
b)Electronic mail: zhihongl@uci.edu

apply a mature, benchmarked turbulence simulation, the Gyrokinetic Toroidal Code (GTC)[41,42] to the FRC with realistic parameters from the C-2 experiment. GTC has been successfully applied to simulate microturbulence,[43] energetic particle transport,[44] Alfvén eigenmodes,[45,46] and magnetohydrodynamic (MHD) instabilities, including the kink mode[47] and tearing mode[48] in fusion plasmas. This paper details the necessary upgrades which have been made to GTC to carry out simulations of an FRC.

In this study, a formulation for gyrokinetic particle simulation of the FRC is presented, with emphasis on the construction of a field-aligned mesh using magnetic Boozer coordinates[49,50] and the implementation of a field solver in the FRC magnetic geometry. As a first step in developing FRC simulation capabilities, this study is confined to electrostatic effects. Electromagnetic instabilities, demonstrated to be relevant in FRC plasmas,[25,27,51] will be investigated in detail in a future study, and the authors note that electromagnetic capabilities are already present in the GTC framework.[41,52–54] Verifications carried out on the newly implemented features are noted and results from first simulations are presented. Initial simulations find a pressure-gradient-driven driftwave instability on the ion scale in the SOL. Most interestingly, the ion scale driftwave is stabilized in the core by the large ion gyroradius.[55]

In Section II, we develop a coordinate mapping algorithm to produce magnetic Boozer coordinates from an MHD equilibrium in cylindrical coordinates. We also detail an extension of these Boozer coordinates into the SOL, constituting the first open field line simulation domain for GTC. Section III explains modifications to the field solver to accommodate the FRC's poloidal-only magnetic field. We demonstrate some initial simulation results in Section IV, in both the FRC core and SOL. Finally, conclusions, discussion, and direction of future efforts are presented in Section V.

II. MAPPING TO MAGNETIC BOOZER COORDINATES IN AN FRC MAGNETIC FIELD GEOMETRY

There are a number of advantages to using *magnetic-flux coordinates* in a particle-in-cell simulation of magnetically confined plasma. Magnetic-flux coordinates are obtained by applying the constraint that the constant coordinate surfaces of one coordinate, typically referred to as the "radial coordinate," correspond to the surfaces traced out by magnetic field lines. Such a coordinate system greatly simplifies expressions for physical quantities, such as the magnetic field, **B**, and electric current, **J**. Plasma equilibrium quantities, including density, temperature, and pressure, are uniform on a magnetic flux surface and thus can be expressed as one-dimensional profiles using flux coordinates. Applying a second constraint on a magnetic-flux coordinate system, namely, that magnetic field lines are straight in the plane of the remaining two coordinates, results in *straight field line coordinates*. Advantages to using straight field line coordinates are manyfold. One such advantage is the ability to represent the magnetic field with scalar functions. Another advantage is having a field-aligned computational mesh,

which simplifies the implementation of the field solver and particle equations of motion and minimizes the grid number required to resolve unstable modes, which are typically elongated along magnetic field lines. For any such flux coordinates, the magnetic field may be expressed in terms of coordinate gradients, $\mathbf{B} = \nabla\psi_{\mathrm{tor}} \times \nabla\theta + \nabla\psi_{\mathrm{pol}}^{\mathrm{r}} \times \nabla\zeta$, where ψ_{tor} is the toroidal flux and $\psi_{\mathrm{pol}}^{\mathrm{r}}$ is the poloidal flux. Represented in this form, the magnetic field is automatically divergence-free and the existence of flux surfaces is guaranteed.

A third constraint is still required to establish a unique coordinate system. One common choice is to require that the periodic part of the magnetic scalar potential goes to zero, resulting in a simplified expression for the coordinate Jacobian. This particular choice, established by Boozer in the early 1980s, is referred to as *magnetic Boozer coordinates*.[56] The simplified form of the Jacobian appears as $\mathcal{J} = (qI_{\mathrm{pol}} + I_{\mathrm{tor}})/B^2$, where I_{pol} is the poloidal current, I_{tor} is the toroidal current, and q is the safety factor. These terms will be explained in greater depth in Section II B.

GTC is formulated using Boozer coordinates, so the first step in implementing FRC simulation capabilities is producing a mapping algorithm to translate FRC equilibria from cylindrical coordinates into magnetic Boozer coordinates. The mapping algorithm is most easily formulated by division into three stages. First, we map from the cylindrical coordinates, given as input from an MHD equilibrium code, to any set of magnetic-flux coordinates. Second, we establish a system of straight field line coordinates from the initial magnetic-flux coordinates. Third, we develop a transformation from the straight field line coordinates to the unique Boozer coordinates. With this three-stage coordinate mapping, we may interpolate values of the needed physical quantities onto the new grid in GTC.

One important note in establishing this algorithm is that the coordinate transformation only needs to be performed once for a given equilibrium, and the output may be saved. This work flow makes run-time efficiency of the coordinate mapping a relatively low priority. Numerical fidelity, by comparison, is critical, since the self-consistency of the equilibrium magnetic field will affect the numerical accuracy of the particle push and field solver in every time step of the simulation.

In the remainder of this section, we present an implementation of coordinate mapping from cylindrical coordinates to Boozer magnetic coordinates, including simplifications specific to FRC magnetic field geometry and verifications.

A. Input to the coordinate mapping

The input magnetic equilibrium to the coordinate mapping algorithm is generated by a 2-D equilibrium code, LR_eqMI, developed at TAE.[57] The code LR_eqMI is designed to model equilibria in plasmas with multiple ion species. It allows for realistic boundary conditions with any combination of electrically conducting or insulating walls in an arbitrary geometry.

This input includes the magnitude and vector direction of the magnetic field on a cylindrical coordinate grid, (R, Z, ζ), where

$$\{R \in \mathbb{R} \, | \, 0 < R < \infty\}$$
$$\{Z \in \mathbb{R} \, | -\infty < Z < \infty\}$$
$$\{\zeta \in \mathbb{R} \, | \, 0 \leq \zeta < 2\pi\}.$$

Cartesian coordinates may be related back to these cylindrical coordinates via the expression

$$x = R \cos \zeta$$
$$y = Z$$
$$z = R \sin \zeta. \tag{1}$$

Note that this definition is different from the conventional cylindrical coordinates, (r, θ, z). To maintain right-handedness, the direction of the angular coordinate is reversed relative to convention. A number of physical quantities may be optionally included in the LR_eqMI equilibrium. The mapping algorithm requires only the magnetic flux, $\psi_{\text{pol}}^{\text{r}}$ and the vector magnetic field in cylindrical coordinates, $\mathbf{B} = (B_R, B_Z, B_\zeta)$. Plasma parameters, including ion density, electron density, ion temperature, and electron temperature, are taken from the LR_eqMI equilibrium grid to produce one-dimensional plasma profiles which are used directly as GTC input.

The top panel of Fig. 2 shows the cylindrical input grid, which is symmetric in ζ, in the R–Z plane, along with color contours of the flux surfaces.

B. Establishing flux coordinates and straight field line coordinates

A magnetic flux surface is a smooth surface such that $\mathbf{B} \cdot \mathbf{n} = 0$ everywhere, where $\mathbf{n}$ is a perpendicular to the surface. In a toroidal field geometry, these surfaces are nested and donut shaped. The innermost surface, as the donut narrows to a ring, is designated as the *magnetic axis*. Flux coordinates use these surfaces to represent one position in three-dimensional coordinate space.

The first step in developing the desired mapping algorithm is establishing some set of flux coordinates. As designated in Section II A, our initial cylindrical coordinate system is (R, Z, ζ). These cylindrical coordinates may be simply transformed into toroidal coordinates, a donut-shaped coordinate system conventionally used for toroidal geometries, denoted (r, θ, ζ), where

$$r = \sqrt{(R - R_0)^2 + Z^2}$$
$$\theta = \arctan(Z/(R - R_0))$$
$$\zeta = \zeta. \tag{2}$$

The R_0 in (2) is the R location of the magnetic axis, and is easily obtained from the LR_eqMI input equilibrium by locating the minimum flux value. The $\hat{r}$, $\hat{\theta}$, and $\hat{\zeta}$ components of vector quantities are, respectively, referred to as *radial*, *poloidal*, and *toroidal*, and this nomenclature carries

over to topologically similar coordinate systems, such as those discussed in the remainder of this paper.

Obtaining magnetic flux coordinates requires replacing the radial coordinate, r, with a flux surface label, ψ. As mentioned in Section II A, this magnetic flux is supplied on the cylindrical grid in the input to the mapping algorithm. Specifically, we have the poloidal flux as a function of cylindrical coordinates, $\psi_{\text{pol}}^{\text{r}}(R, Z)$. Here, "poloidal" refers to the poloidal component of magnetic field, which is integrated over a surface, S_p, a ring-shaped ribbon in the $r - \zeta$ plane, stretched from the magnetic axis to the flux surface of interest.

$$\psi_{\text{pol}}^{\text{r}} = \int_{S_p} \mathbf{B} \cdot \mathbf{dS}.$$

This flux may be used in place of r in the toroidal coordinates expressed in (2). One feature of the FRC geometry is symmetry in the coordinate ζ which means establishing the radial flux coordinate is a matter of simple 2-D interpolation on the R–Z coordinate plane.

The second step in developing a mapping algorithm is obtaining *straight field line coordinates*, which we denote with a subscript "f." Straight field line coordinates are a set of magnetic flux coordinates, $(\psi_{\text{f}}, \theta_{\text{f}}, \zeta_{\text{f}})$, such that magnetic field lines drawn in the $\theta_{\text{f}} - \zeta_{\text{f}}$ plane are straight lines. In the general case, establishing a set of straight field line coordinates from arbitrary flux coordinates may be quite involved. FRCs, however, contain *only* poloidal magnetic field, that is to say, $B_\zeta = 0$, so magnetic field lines drawn in the $\theta - \zeta$ plane are already straight, horizontal lines. Therefore, the set of magnetic flux coordinates which we have already established is also a set of straight field line coordinates in an FRC geometry. Our straight field line flux coordinate now looks like

$$\psi_{\text{f}} = \psi_{\text{pol}}^{\text{r}}(R, Z)$$
$$\theta_{\text{f}} = \theta$$
$$\zeta_{\text{f}} = \zeta. \tag{3}$$

C. Determining Boozer coordinates from straight field line coordinates

The formal derivation of Boozer coordinates is well established, and we leave it to the reader to procure the details from a previous publication. We recommend the text by D'haeseleer *et al.*, which provides a general treatment for the derivation of Boozer coordinates along with a myriad of other flux coordinate choices.[50] Here, we summarize the result for the general case

$$\psi_{\text{B}} = \psi_{\text{f}}$$
$$\theta_{\text{B}} = \theta_{\text{f}} + \dot{\psi}_{\text{pol}}^{\text{r}} \frac{2\pi}{\mu_0} \frac{\tilde{\Phi}}{\dot{\psi}_{\text{pol}}^{\text{r}} I_{\text{tor}} + \dot{\psi}_{\text{tor}} I_{\text{pol}}}$$
$$\zeta_{\text{B}} = \zeta_{\text{f}} + \dot{\psi}_{\text{tor}} \frac{2\pi}{\mu_0} \frac{\tilde{\Phi}}{\dot{\psi}_{\text{pol}}^{\text{r}} I_{\text{tor}} + \dot{\psi}_{\text{tor}} I_{\text{pol}}}, \tag{4}$$

where μ_0 is the permeability of free space, $\dot{\psi}_{\text{tor}}$ is the derivative of the toroidal flux with respect to ψ_{f}, $\dot{\psi}_{\text{pol}}^{\text{r}}$ is the

derivative of the poloidal flux with respect to ψ_f, and $\tilde{\Phi}$ is the periodic part of the magnetic scalar potential. Here, we have chosen the radial flux coordinate $\psi^r_{pol} = \psi_f$ so the value of $\dot{\psi}^r_{pol} = 1$. The toroidal flux, ψ_{tor}, on a flux surface labelled ψ_f is the toroidal magnetic field component integrated over a surface, S_t, in the $\psi_f - \theta_f$ plane contained within the flux surface of interest,

$$\psi_{tor} = \int_{S_t} \mathbf{B} \cdot \mathbf{dS}.$$

The magnetic scalar potential, Φ, is the homogeneous solution to Ampere's law, that is

$$\mu_0 \mathbf{J} = \nabla \times \mathbf{B}$$
$$= \nabla \times (\nabla\Phi + \mathbf{B}_j) \quad \text{where}$$
$$0 = \nabla \times \nabla\Phi$$
$$\mu_0 \mathbf{J} = \nabla \times \mathbf{B}_j.$$

It may be composed of both constant and periodic parts, $\Phi = \Phi_0 + \tilde{\Phi}$, of which we are only interested in the periodic portion, $\tilde{\Phi}$.

In the case of FRC magnetic geometry, simplifications to Eq. (4) may be considered. First, since there is no toroidal magnetic field, the toroidal flux and its derivatives are zero, $\psi_{tor} = \dot{\psi}_{tor} = 0$. Correspondingly, there may only be equilibrium current in the toroidal direction and thus the poloidal current is also zero, $I_{pol} = 0$. Making these substitutions, (4) becomes

$$\psi_B = \psi_f$$
$$\theta_B = \theta_f + \frac{2\pi}{\mu_0} \frac{\tilde{\Phi}}{I_{tor}}$$
$$\zeta_B = \zeta_f. \tag{5}$$

Combining (5) and (3), we can write our fully simplified Boozer coordinate transformation in an FRC magnetic field geometry

$$\psi_B = \psi^r_{pol}(R, Z)$$
$$\theta_B = \arctan\left(\frac{Z}{R - R_0}\right) + \frac{2\pi}{\mu_0} \frac{\tilde{\Phi}(\psi^r_{pol}(R, Z), \theta_f, \zeta_f)}{I_{tor}}$$
$$\zeta_B = \zeta. \tag{6}$$

Notably, the periodic magnetic scalar potential, $\tilde{\Phi}$, is left in terms of θ_f and ζ_f since we are considering the periodicity *in the straight field line coordinates*. All of the quantities on the right hand side of this transformation are physical and may be determined from the information given on the input cylindrical mesh from LR_eqMI.

To implement the coordinate transformation, numerical values for ψ^r_{pol}, $\tilde{\Phi}$, and I_{tor} must be determined. The poloidal flux, ψ^r_{pol}, is provided directly in the LR_eqMI input, but the others must be computed. If we consider the covariant expression of the magnetic field, $\mathbf{B}$, the directional components of $\mathbf{B}$ contain both $\tilde{\Phi}$ and I_{tor} terms:

$$\mathbf{B} = \left(-\mu_0 \tilde{\eta} + \frac{\partial\tilde{\Phi}}{\partial\psi_f}\right) \nabla\psi_f$$
$$+ \left(\frac{\mu_0}{2\pi} I_{tor} + \frac{\partial\tilde{\Phi}}{\partial\theta_f}\right) \nabla\theta_f$$
$$+ \left(\frac{\mu_0}{2\pi} I_{pol} + \frac{\partial\tilde{\Phi}}{\partial\zeta_f}\right) \nabla\zeta_f. \tag{7}$$

Since there is no toroidal field in FRC geometry, the $\nabla\zeta_f$ component of $\mathbf{B}$ is zero. This gives

$$\frac{\mu_0}{2\pi} I_{pol} + \frac{\partial\tilde{\Phi}}{\partial\zeta_f} = 0. \tag{8}$$

As noted, $I_{pol} = 0$, and therefore $\partial\tilde{\Phi}/\partial\zeta_f = 0$ must also be true. The magnetic scalar potential, $\tilde{\Phi}$, has no ζ_f dependence, which is expected since we still have axisymmetry in the straight field line coordinates.

The $\nabla\theta_f$ component of $\mathbf{B}$ is non-zero

$$B_{\theta_f} \equiv \frac{|\mathbf{B} \times \nabla\psi_f|}{|\nabla\psi_f \times \nabla\theta_f|} = \frac{\mu_0}{2\pi} I_{tor} + \frac{\partial\tilde{\Phi}}{\partial\theta_f}. \tag{9}$$

The B_{θ_f} term on the left-hand side of (9) may be computed directly by expressing the terms in cylindrical coordinates. Doing so yields

$$B_{\theta_f} \equiv \frac{\left|\left(B_R\hat{R} + B_Z\hat{Z} + B_\zeta\hat{\zeta}\right) \times \left(\frac{\partial\psi_f}{\partial R}\hat{R} + \frac{\partial\psi_f}{\partial Z}\hat{Z} + \frac{\partial\psi_f}{\partial\zeta}\hat{\zeta}\right)\right|}{\left|\left(\frac{\partial\psi_f}{\partial R}\hat{R} + \frac{\partial\psi_f}{\partial Z}\hat{Z} + \frac{\partial\psi_f}{\partial\zeta}\hat{\zeta}\right) \times \left(\frac{\partial\theta_f}{\partial R}\hat{R} + \frac{\partial\theta_f}{\partial Z}\hat{Z} + \frac{\partial\theta_f}{\partial\zeta}\hat{\zeta}\right)\right|}$$
$$= \frac{\mu_0}{2\pi} I_{tor} + \frac{\partial\tilde{\Phi}}{\partial\theta_f}. \tag{10}$$

Using the relationship expressed in (3), partial derivatives may be numerically computed everywhere.

Because $\tilde{\Phi}$ is periodic in θ_f, the derivative, $\partial\tilde{\Phi}/\partial\theta_f$, cannot have a constant component. By contrast, I_{tor} is a flux function and is constant with respect to θ_f. By applying a discrete Fourier transform to the total term, B_{θ_f}, the constant and oscillatory parts can be separated as Fourier components, giving values for I_{tor} and $\partial\tilde{\Phi}/\partial\theta_f$, respectively.

In our implementation, the forward and inverse Fourier transforms of B_{θ_f} take the form

$$B_k = \sum_{j=1}^{N} B_j e^{(-2\pi\iota)(j-1)(k-1)/N}$$
$$B_j = \frac{1}{N} \sum_{k=1}^{N} B_k e^{(2\pi\iota)(j-1)(k-1)/N}. \tag{11}$$

Here, the real-space function is $B_j = B_{\theta_f}(\theta_f(j))$, where $\theta_f(j) = 2\pi(j-1)/N$. The k-space function is represented by B_k, where $k = 1$ represents the constant component and $k = 2, 3, 4, \ldots$ represent higher oscillatory harmonics. To ensure good numerical resolution, the number of grid points, N, of the intermediary straight field line grid, B_{θ_f}, is at least a

factor of five greater than the desired number of grid points in the final Boozer coordinate mesh.

To obtain the toroidal current, I_{tor}, only the constant component is kept from the transform

$$\frac{\mu_0}{2\pi} I_{\text{tor}}(\psi_{\text{f}}, \theta_{\text{f}}(j)) = \frac{1}{N} \sum_{k=1}^{1} B_k e^{(2\pi\iota)(j-1)(k-1)/N}$$

$$= \frac{1}{N} B_{k=1}$$

$$= \frac{1}{N} \sum_{j=1}^{N} B_j e^0$$

$$I_{\text{tor}}(\psi_{\text{f}}) = \frac{2\pi}{\mu_0 N} \sum_{j=1}^{N} B_{\theta_{\text{f}}}(\theta_{\text{f}}(j)). \qquad (12)$$

Now the results in (12) and (13) are simply plugged into transformation (6), and the cylindrical to Boozer coordinate transformation algorithm is established.

D. Output requirements from the coordinate mapping

The code which we are modifying for the FRC simulation, GTC, is formulated to push particles and solve electric and magnetic fields in Boozer coordinates. The desired output of the mapping algorithm is a coordinate grid system, regularly spaced in Boozer coordinates, with the cylindrical coordinate location of each of these new grid points. This constitutes an inverse coordinate mapping, $R(\psi_{\text{B}}, \theta_{\text{B}}, \zeta_{\text{B}})$, $Z(\psi_{\text{B}}, \theta_{\text{B}}, \zeta_{\text{B}})$, and $\zeta(\psi_{\text{B}}, \theta_{\text{B}}, \zeta_{\text{B}})$, from Boozer to cylindrical coordinates. These inverse coordinate transformations are used for gyroaveraging and computation of the metric tensor in GTC. Using splines, they also provide a quick method to determine a cylindrical position from a given Boozer coordinate location, which is practical for plotting diagnostics and comparison to experiments.

A series of one-dimensional high-resolution splines are used to implement the inverse transformation. For a given flux surface, a set of regularly spaced θ is generated, and corresponding θ_{B} are produced using (3) and (5). From these values, a one-dimensional spline of $\theta(\theta_{\text{B}})$ is generated on the flux surface, and this spline is used to determine θ values at the desired, regularly spaced θ_{B} positions. This must be done for every flux surface of interest, so regularly spaced values of ψ_{B} are selected to be sampled from the LR_eqMI input from

Notably, there is no j dependence in the final expression since we keep only the $k = 1$ term. As expected, I_{tor} is a flux surface constant.

We need to integrate the partial derivative term from (10) to obtain $\tilde{\Phi}$. Integrating around the flux surface in real space aggregates numerical error, so the total error in $\tilde{\Phi}$ near $\theta_{\text{f}} = 2\pi$ would become large. By taking advantage of the Fourier transform and integrating in k-space instead, these numerical issues are avoided. Applying the Fourier transform, the integration operator becomes

$$\int d\theta_{\text{f}} \rightarrow \frac{-\iota}{k - 1}.$$

Keeping only the oscillatory components, the complete magnetic scalar potential looks like

$$\tilde{\Phi}(\psi_{\text{f}}, \theta_{\text{f}}(j)) = \frac{1}{N} \sum_{k=2}^{N} \frac{-\iota}{k-1} B_k e^{(2\pi\iota)(j-1)(k-1)/N}$$

$$= \frac{1}{N} \sum_{k=2}^{N} \left(\frac{-\iota}{k-1} \sum_{j'=1}^{N} \left(B_{j'} \times e^{(-2\pi\iota)\,(j'-1)\,(k-1)/N} \times e^{(2\pi\iota)\,(j-1)\,(k-1)/N} \right) \right)$$

$$\tilde{\Phi}(\psi_{\text{f}}, \theta_{\text{f}}(j)) = \frac{1}{N} \sum_{k=2}^{N} \sum_{j'=1}^{N} \left(\frac{-\iota}{k-1} B_{\theta_{\text{f}}}\left(\theta_{\text{f}}(j')\right) \times e^{(2\pi\iota)(j-j')\,(k-1)/N} \right). \qquad (13)$$

the beginning of the mapping algorithm. Looking at Eq. (6) makes it apparent that most of the complexity of the coordinate mapping algorithm is contained in the relation between θ and θ_{B}. Fig. 1 shows a sample of the relationship between θ and θ_{B} on a reference flux surface. A similar one-dimensional spline may be formed on a given straight radial ray in toroidal coordinates which corresponds to a single θ. First, a set of regularly spaced r is generated. With θ fixed, each r corresponds to a single flux value, giving the spline, $r(\psi_{\text{B}})$.

The physical values of magnetic field magnitude, density, and temperature are also needed on the new grid. Once the (R, Z) coordinate locations are obtained for the regularly spaced Boozer grid, these physical quantities are simply interpolated from the original LR_eqMI input file using a standard 2-D interpolation algorithm.

E. Extension of Boozer coordinates in the SOL

Understanding transport in the scrape-off-layer is critical to understanding global FRC transport. Because the SOL acts as a divertor, transport behaviour inside and outside of the separatrix is qualitatively different.

A major obstacle to using GTC for simulations of the SOL is that magnetic Boozer coordinates are not defined for open magnetic field lines. Since the field lines in the region are not closed, the *periodic* magnetic scalar potential becomes meaningless. For equilibria that are symmetric over the $Z = 0$ axis, which is approximately true for C-2, one solution is to enforce periodicity across the Z boundary when
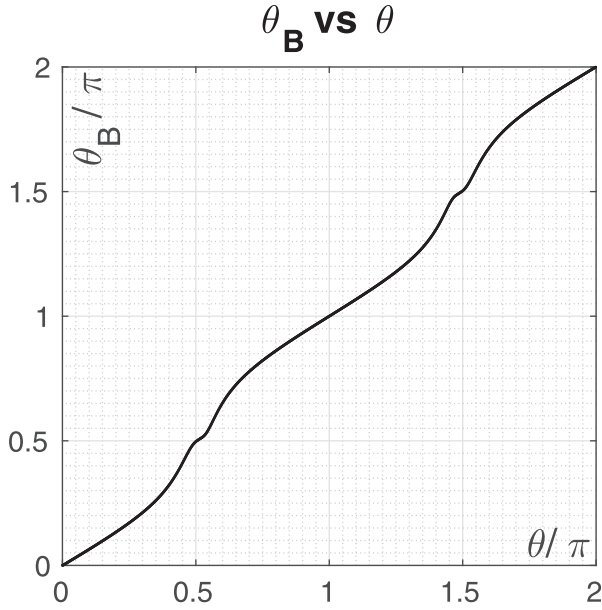
θ_B vs θ

FIG. 1. Mapping from the geometry poloidal angle, θ, to the Boozer coordinate poloidal angle, θ_B on a reference flux surface.

performing the Fourier decomposition on each flux surface. This provides a consistent coordinate system to use in the SOL. Note that enforcing this periodicity for the coordinate transformation is distinct from the choice of boundary conditions applied to the field solver and particle equations of motion during the simulation, which is discussed in Section III. One consequence of enforcing periodicity during the coordinate mapping is that the spacing of the poloidal θ_B-coordinate in the SOL is dependent on the length, in Z, of the simulation domain. A wider domain in Z will produce larger spacing between constant-θ_B surfaces. This means that necessarily, θ_B is discontinuous across the separatrix. Consequently, simulations may be carried out separately in the core *or* the SOL but not both simultaneously.

With this implementation of SOL coordinates, the description of Boozer coordinates in FRC geometry is complete. The method outlined in this subsection is sufficient to investigate

transport isolated in the SOL. The effects of core-SOL coupling are also of critical interest and will be investigated with a different model in future work. Progression of the coordinate mapping from cylindrical to straight field line to Boozer coordinates in the core and SOL is illustrated in Fig. 2.

III. FORMULATION OF POISSON SOLVER IN FRC GEOMETRY

We begin by introducing the electrostatic gyrokinetic equations[58] to describe a toroidal plasma in an inhomogeneous magnetic field, using the gyrocenter position, $\mathbf{X}$, magnetic moment, μ, and parallel velocity, $v_\parallel$, as a set of independent variables

$$\frac{d}{dt}f_\alpha(\mathbf{X}, \mu, v_\parallel, t) \equiv \left[\frac{\partial}{\partial t} + \dot{\mathbf{X}} \cdot \nabla + \dot{v}_\parallel \frac{\partial}{\partial v_\parallel} - C_\alpha \right] f_\alpha, \quad (14)$$

$$\dot{\mathbf{X}} = v_\parallel \frac{\mathbf{B}_0}{B_0} + \mathbf{v}_E + \mathbf{v}_d, \quad (15)$$

$$\dot{v}_\parallel = -\frac{1}{m_\alpha} \frac{\mathbf{B}_0^*}{B_0} \cdot (\mu \nabla B_0 + Z_\alpha \nabla \phi) - \frac{Z_\alpha}{m_\alpha c} \frac{\partial A_\parallel}{\partial t}. \quad (16)$$

The subscript, $\alpha = e, i$, represents the particle species, either ions or electrons. The effective magnetic field is

$$\mathbf{B}_0^* = \mathbf{B}_0 + \frac{B_0 v_\parallel}{\Omega_\alpha} \nabla \times \mathbf{b}_0. \quad (17)$$

The additional velocity terms are the $E \times B$ drift velocity, $\mathbf{v}_E$, and the magnetic drift velocity, v_d, which is the sum of the magnetic curvature drift and the ∇B drift. In the perturbative (δf) simulation,[59–62] the distribution function, f_α, may be broken into an equilibrium part, f_0, and a perturbed part, δf, such that $f_\alpha = f_0 + \delta f$. Corresponding to the distribution function, we can define perturbed gyroaveraged densities for each species of particle

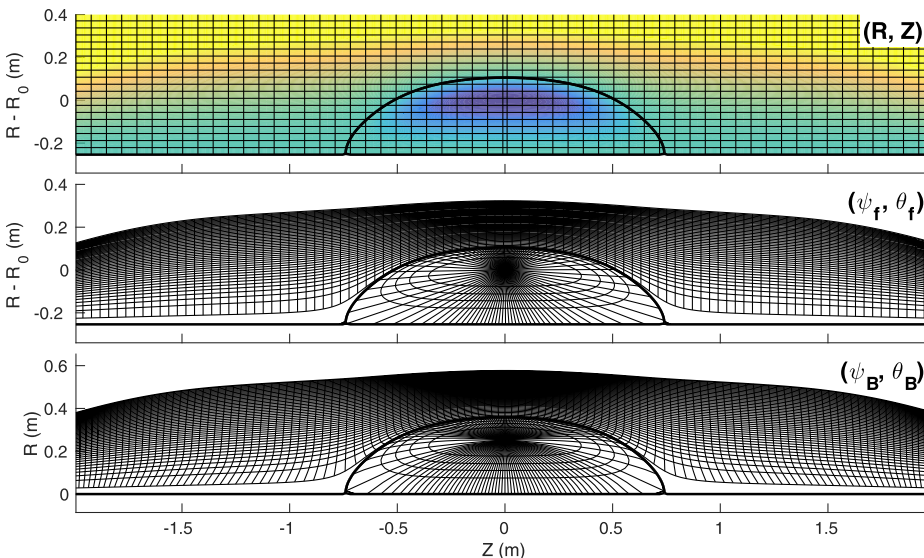$$\overline{\delta n_\alpha} = \int \delta f_\alpha d^3 v. \quad (18)$$

FIG. 2. Poloidal plane meshes for three coordinates systems. In the top panel, cylindrical coordinates, (R, Z), with contours beneath showing magnetic flux extracted from the LR_eqMI input equilibrium. In the middle panel, the straight field line coordinate mesh, (ψ_f, θ_f). In the bottom panel, Boozer coordinates, (ψ_B, θ_B) are shown. The separatrix is indicated by the wide black line.

The difference between the magnetic geometries of the tokamak and FRC makes it necessary to reformulate the Poisson solver. In the gyrokinetic formulation, electric and magnetic fields are solved on the plane perpendicular to magnetic field lines. In tokamaks, the field is primarily toroidal with a small poloidal component, while in FRCs, the field is entirely poloidal. GTC has several methods for solving the Poisson equation,[63] and for the FRC, we solve the gyrokinetic Poisson equation with the Padé approximation. The normalized form of the gyrokinetic Poisson equation and its representation in FRC geometry may be expressed as

$$\nabla_\perp^2 \Phi = (1 - \nabla_\perp^2)(\overline{\delta n_i} - \overline{\delta n_e}), \tag{19}$$

$$= \left(g^{\psi\psi} \frac{\partial^2}{\partial \psi^2} + g^{\zeta\zeta} \frac{\partial^2}{\partial \zeta^2} \right) \Phi, \tag{20}$$

where δn_i is the perturbed ion density, δn_e is the perturbed electron density, Φ is electrostatic potential, and $g^{\xi^\alpha \xi^\beta} \equiv \nabla \xi^\alpha \times \nabla \xi^\beta$ is the metric tensor element.[63]

Our initial focus is on the linear properties of FRC instabilities. In this work, we present simulations of single-n modes, where n, the toroidal mode number, is an integer related to the mode's toroidal wave number by $k_{\text{tor}} = n/R_0$. Characterizing linear instabilities in the FRC requires parameter scans consisting of many such single-n simulations. To make these scans feasible, we implement optimizations in the Poisson solver. The first optimization is the reduction of the toroidal simulation domain to a partial-torus which eliminates grid size dependence on the toroidal mode number as detailed in Section III A. The gyro-kinetic treatment of particles is detailed in Section III B. In Section III C, the second optimization, the semi-spectral operator used to solve the gyrokinetic Poisson equation, is outlined.

A. Partial torus domain

To accurately resolve shorter toroidal wavelength modes, a finer simulation grid is necessary, incurring higher computational costs. We make use of the toroidal periodicity of single-n modes to attain a computational cost that is independent of the toroidal mode number, n, in the linear simulation of a single n mode.

The computational cost of a simulation is proportional to the number of grid points used. In the field solver, increased number of grid points means that the matrix representing the Laplacian operator becomes larger. For fixed particles per grid cell, the total number of particles in the simulation is also proportional to the number of grid points. In a full torus, the total number of grid points is a product of grid points per wavelength and wavelengths per torus. While grid points per wavelength determines how well the mode in question is resolved, wavelengths per torus adds computational cost without benefit. The periodicity of a single-n mode in the toroidal direction allows reduction of the domain size from a full torus, $[0, 2\pi]$, to a partial torus, $[0, 2\pi/n]$. This partial torus domain corresponds to one wavelength of the mode. Implementation of

this scheme requires only minor modification of the particle boundary conditions, which are already periodic in the full torus case. Particles passing out through 0 enter from $2\pi/n$ and vice versa. The mode can now be well resolved without sacrificing computational efficiency. The total number of particles, particles per wavelength, number of grid points per wavelength and, correspondingly, computational cost and mode resolution are all independent of the mode wavelength.

In future non-linear simulations, when inclusion of multiple n modes is desirable, the partial torus domain may still be used to sample a single toroidal mode number plus its harmonics: 0, n, 2n, 3n,. The full torus domain will be applied in instances where all n modes are kept.

B. Gyroaveraging

For turbulence and transport, the plasma phenomena of interest often evolve on a time-scale longer than the ion gyro-period. The salient feature of gyrokinetic formulations is averaging over the gyro-phase angle, which reduces the phase space dimensionality from six dimensions to five dimensions and allows a much coarser simulation time step. In order to retain realistic finite Larmour radius effects, we must perform accurate gyro-averaging on particles.

In the FRC implementation, the gyro-average of a function is split into radial gyro-averaging and toroidal gyro-averaging. In the toroidal direction, spatial sampling is expensive, because domain decomposition requires message passing between toroidal neighbors. Fortunately, when simulating single-n modes, mode variation in the toroidal direction is simple and easy to approximate. By contrast, spatial sampling in the radial direction does *not* require expensive communication, but all radial wave numbers are retained making approximation of the radial mode variation impractical. These qualitative differences lead us to treat the two dimensions separately.

Radial gyro-averaging is represented by gyro-particles sampling different locations of the gyro-ring. In the case where the radial and toroidal wavenumbers are similar in magnitude, $k_r \sim k_\zeta$, radial two-point averaging may be used to include gyroaveraged effects.[64] In radially local simulations, where $k_r \ll k_\zeta$, radial gyro-averaging is omitted, since its effects are negligible. In both cases, toroidal gyro-averaging is represented as the multiplication of a Bessel function of the first kind $J_0(k_\zeta \rho_c)$, where the arguments are $k_\zeta = n/R$ and $\rho_c = mv_\perp/|q|B$. Here, n is the toroidal mode number, R is the major radius measured from the machine axis to the particle position, m is the particle mass, q is the particle charge, $v_\perp$ is the particle velocity perpendicular to the magnetic field, and B is the magnetic field strength at the particle position. The value of the Bessel function is calculated using an intrinsic Fortran function for each individual particle, and the multiplication of this factor is self-consistently applied to each particle in the accumulation of the charge density on the grid and in the time-advancement of particle positions. Timing tests indicate that use of the Fortran intrinsic Bessel function does not significantly affect

the simulation runtime. In future simulations, with increased number of particles, if the current implementation becomes a bottleneck, the Bessel functions may be implemented more efficiently by table look-up.

C. Semi-spectral operator

Taking advantage of the toroidal periodicity, we Fourier-decompose in the $\hat{\zeta}$ direction to obtain the semi-spectral Laplacian operator

$$f(\psi, \theta, \zeta) \rightarrow \hat{f}(\psi, \theta)e^{-in\zeta}$$

$$\frac{\partial}{\partial \zeta} \rightarrow -in$$

$$\nabla_\perp^2 \rightarrow \nabla_n^2 = g^{\psi\psi}\frac{\partial^2}{\partial\psi^2} - g^{\zeta\zeta}n^2. \quad (21)$$

Numerically, the derivative in the $\hat{\psi}$ direction is still found by central finite differencing, where i is the grid index corresponding to ψ

$$\nabla_n^2 = g^{\psi\psi}(\phi_{i+1} - 2\phi_i + \phi_{i-1}) - g^{\zeta\zeta}n^2\phi_i$$
$$= g^{\psi\psi}(\phi_{i+1} + \phi_{i-1}) - (2\,g^{\psi\psi} + n^2\,g^{\zeta\zeta})\phi_i. \quad (22)$$

Because one of the perpendicular directions is $\hat{\zeta}$, this results in a tri-diagonal matrix with total number of non-zero elements equal to $3 \times N_\psi$ and a total matrix size of N_ψ^2 which is solved using the Krylov method implemented in PETSc.[65] Here, N_ψ is the number of radial grid points, N_θ is the number of poloidal grid points, and N_ζ is the number of toroidal grid points. The general process of solving the Poisson equation is summarized in the following:

(1) Density is split into $\psi - \zeta$ planes of size $N_\psi \times N_\zeta$ to processors based on θ value assigned to individual processor;
(2) Transform density planes of size $N_\psi \times N_\zeta$ by FFT to semi-spectral density on $\psi - n$ planes of size $(N_\psi \times N_\zeta)/2 + 1$;
(3) Semi-spectral potential is found on each $\psi - n$ plane of size $(N_\psi \times N_\zeta)/2 + 1$ by PETSc;
(4) Semi-spectral potential on $\psi - n$ plane of size $(N_\psi \times N_\zeta)/2 + 1$ is transformed back by FFT^{-1} to real-space potential in $\psi - \zeta$ plane of size (mpsi × mtoroidal), keeping only n of interest non-zero;
(5) Potential on $\psi - \zeta$ plane of size $N_\psi \times N_\zeta$ is passed back to every processor to construct 3D potential of size $N_\psi \times N_\zeta \times N_\theta$;

IV. INITIAL SIMULATION RESULTS

In this section, we report on initial simulation of drift-wave instabilities in the FRC, using the newly implemented code features described in Sections II and III. More detailed physics analysis will be reported in a forthcoming publication.[66] Prior to these simulations, simple test cases were run using both the new implementation and old less efficient (for FRC geometry) algorithms in GTC. We verified that the real frequency and growth rate from both sets of simulations
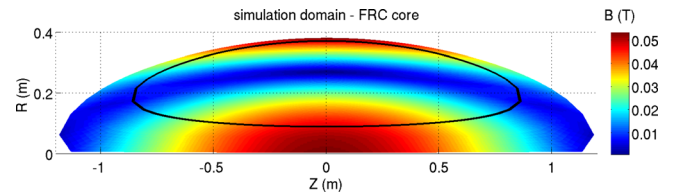

FIG. 3. Simulation domain used in core region.

matched, before undertaking more intensive simulations with the new implementation. Additionally, energy and momentum were recorded over the timescale of the simulation to ensure conservation. The divergence of the magnetic field was computed numerically in the new equilibrium and confirmed to be zero everywhere. The following results come after these verifications.

Linear simulations assume that the toroidal wavelength is much shorter than the radial wavelength of the instabilities, or equivalently, $k_r \ll k_\zeta$. Thus, we can approximate that the radial simulation domain is localized to a single flux surface. This is achieved by modifying the scatter and gather operations such that all dynamics of the system are on the same flux surface. For these single flux surface simulations, the Laplacian operator is further reduced from its spectral form in (21) to $\nabla_n^2 = n^2\,g^{\zeta\zeta}$.

Initial linear simulations are localized to the flux surface where $r/a \approx 0.906$ in the core and $r/a \approx 2.244$ in the SOL, where r is the position of the flux surface relative to the magnetic axis and a is the distance from the separatrix to the magnetic axis, as measured along the mid-plane axis. Radial scans show these locations to be in the region where growth-rates are largest. The domain of the core simulations also excludes the magnetic axis where gyro-kinetic approximations are poor due to the null magnetic field. The simulation domains are shown in Figs. 3 and 4, for the core and SOL, respectively. In future simulations, where the domain is a finite annulus, the radial derivative in the Laplacian operator will be computed via finite differencing.

In the simulations presented in this section, both temperature and density gradient drives are included. The scale length of the gradient of a plasma parameter, f, is $1/L_f = \frac{\partial}{\partial r}\ln(f)$. Here, η characterizes the relative strength of the temperature and density gradients, and is the ratio between the two scale lengths, where $\eta_i = L_{T_i}/L_n$ and $\eta_e = L_{T_e}/L_n$ correspond to ions and electrons, respectively. In these simulations, $\eta_i = \eta_e = \eta = 1$. The simulated ion species is deuterium. Collisional effects were evaluated using the Fokker-Planck model[67] and found to have only small effect on linear growth rates, changing them by less than 10%. For simplicity, collisions are excluded in the following results. The distance from the
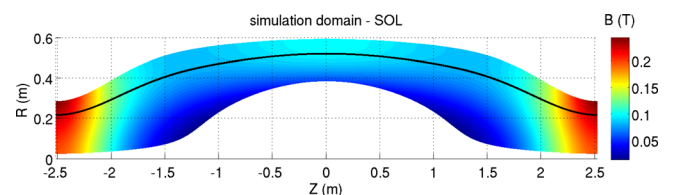

FIG. 4. Simulation domain used in scrape-off layer region.

TABLE I. Equilibrium parameters used in both the core and SOL simulation regions.

	Core	SOL
B_0	533.7 G	2430.5 G
n_e	4.0×10^{13} cm^{-3}	2.0×10^{13} cm^{-3}
T_e	80 eV	40 eV
T_i	400 eV	200 eV
ρ_i	5.3 cm	2.3 cm
ρ_e	0.039 cm	0.017 cm

machine axis to the magnetic axis is $R_0 = 26.96$ cm, and the distance from the magnetic axis to the separatrix on the outer midplane is $a = 11.15$ cm. The simulation parameters and some calculated quantities, including the ion and electron gyro-radii ($\rho_i = \sqrt{m_i T_i}/(eB)$, $\rho_e = \sqrt{m_e T_e}/(eB)$) and sound velocity ($C_s = \sqrt{T_e/m_i}$) are listed in Table I.

Boundary conditions for the particles are reflective on the radial boundaries and periodic on the axial boundary. The field solver assumes a fixed value field on the edges of the grid. Simulations are initialized with particles distributed uniformly across computational cells, with random spatial placement within each cell. The velocity distribution of particles is assumed to be Gaussian about the thermal temperature listed in Table I.

The growth-rates and frequencies of the mode shown in Section IV B are listed alongside the transit frequencies and effective collisionalities in Table II. The transit frequencies of electrons and ions passing along a field-line are $\nu_{tr-e} = V_{th-e}/l$ and $\nu_{tr-i} = V_{th-i}/l$, respectively, where l is the field line length. In the core, the field-line length is estimated by $l = (R_0 + r) * \pi$, and in the SOL, $l \approx 4$ m. For each separate region, the effective collisionalities are listed in Table II. Effective collisionality is the collisional frequency normalized by the transit frequency

$$\nu_{e-e}^* = \nu_{e-e}/\nu_{tr-e}$$
$$\nu_{e-i}^* = \nu_{e-i}/\nu_{tr-e}$$
$$\nu_{i-i}^* = \nu_{i-i}/\nu_{tr-i}.$$

The effective collisionality is quite low for each region due to the short field-line length and the low ion impurity, $Z_{\text{eff}} = 1.5$, in both regions.

TABLE II. Real frequencies, growth rates, characteristic transit frequencies, and effective collisionalities for each species in both the collisionless core and collisional SOL.

	Core	SOL
$\omega_r(R_0/C_S)$	–	9.5
$\gamma(R_0/C_S)$	–	2.3
$\nu_{tr-e}\left(\dfrac{R_0}{C_s}\right)$	5.47	3.23
$\nu_{tr-i}\left(\dfrac{R_0}{C_s}\right)$	2.02×10^{-1}	1.24×10^{-1}
ν_{e-e}^*	1.16	3.81
ν_{e-i}^*	2.45	8.61
ν_{i-i}^*	1.20×10^{-1}	2.61×10^{-1}

A. Simulation of the FRC core

In the core, ion-scale modes are found to be stable. For a mode with wavenumber $k_\zeta \rho_i = 1.0$, the simulation was first run with density and temperature gradients with experimentally realistic values, $R_0/L_n = R_0/L_{T_i} = R_0/L_{T_e} = 2{\sim}4$. When no instability was found, gradient drive was artificially increased to the limits of numerical validity of the gyrokinetic model, but still, no linear instabilities were driven. Possible contributors to mode stabilization are ion finite Larmour radius effects and the magnetic field gradient. Detailed stabilization mechanisms for the ion scale turbulence are under investigation. In general, we expect that higher wavenumber modes are driven more easily than low wavenumber modes. Electron scale turbulence in the core is still under evaluation and will be reported on, in detail in future work.

B. Simulation of the FRC scrape-off layer

In the scrape-off layer, we find unstable ion-scale and electron-scale modes showing typical exponential amplitude growth with real frequency in the ion diamagnetic direction. An unstable collisional mode with $k_\zeta \rho_i = 5.42$ is shown in Fig. 5. The mode is driven by density and temperature gradients, $R_0/L_n = R_0/L_{T_i} = R_0/L_{T_e} = 4.04$, and has real frequency $\omega_r(R_0/C_S) = 9.5$ and growth-rate $\gamma(R_0/C_S) = 2.3$. The conservation of momentum and energy for both ions and electrons is shown in the bottom two panels of Fig. 5.
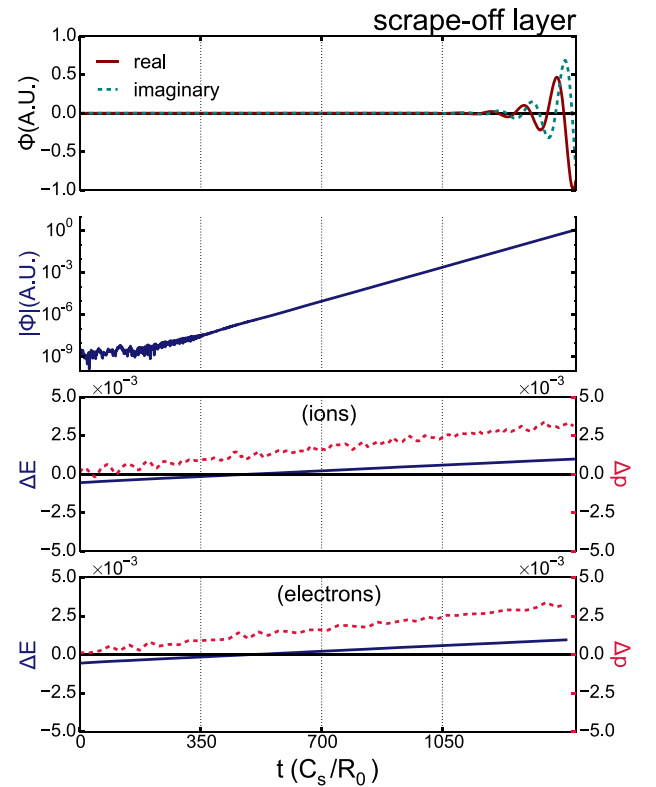

FIG. 5. Time histories of $k_\zeta \rho_i = 5.42$ instability in the FRC SOL. The top two panels show the electrostatic potential in linear and semi-log plots. The bottom two panels show conservation of energy and momentum for each species, with left and right axes corresponding to energy and momentum, respectively.
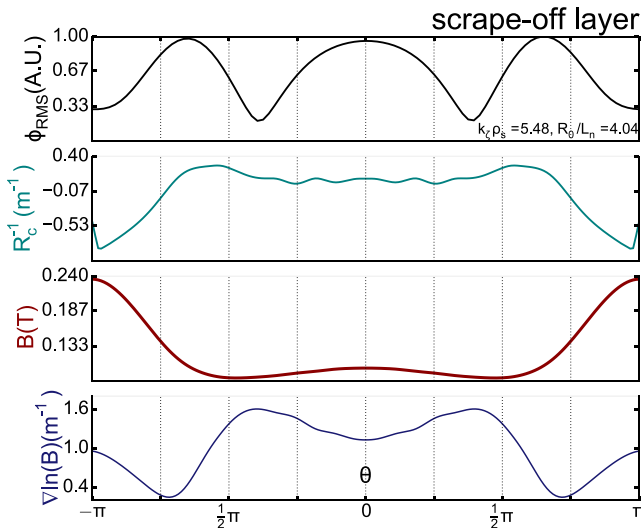
FIG. 6. Mode structure and field geometry of $k_\zeta \rho_i = 5.42$ instability in the FRC SOL versus poloidal angle. From top to bottom, panels show electrostatic potential, field line curvature, magnitude of the magnetic field line, and the radial gradient of the magnetic field.

Overall change in energy and momentum is less than 1% for both species.

The mode structure of the instability is shown in Fig. 6. The mode is characterized by $m = 0$, 1, 2, 3 mode number components. This structure is common to all of the scanned single-n modes in the SOL. The curvature, magnitude of the magnetic field, and the radial gradient of the magnetic field are also shown in Fig. 6. Small-scale fluctuations in the magnetic curvature are due to numerical differencing on the discrete grid. Geometrically, the scrape-off layer region has weaker curvature than the core but a much stronger magnetic field gradient.

Numerical convergence tests have been carried out in the SOL. Mode frequencies converge with only a single particle per cell. Across the entire particle-per-cell convergence scan, the variation in ω is less than 5% and variation in γ is less than 0.1%. The implementation of the partial torus domain allows a significant number of particles per wavelength even in simulations using only one particle per cell. Linear growth rate, γ, converges around a time step size, $\Delta t(R_0/C_s) = 0.005$, while ω shows little variation over the scan. The frequency converges at 64 poloidal grid points, while the growth-rate converges around 128 grid points.

V. DISCUSSION

In this study, a formulation for gyrokinetic particle simulation of a field reversed configuration is presented. A mapping algorithm to produce Boozer magnetic coordinates has been developed and verified, along with an extension of Boozer coordinates into the scrape-off layer region. A formulation for an efficient linear Poisson solver with particle gyroaveraging is also established. All of these new features have been implemented in the GTC, and linear instabilities in an FRC geometry have been simulated.

Initial results from GTC represent, to date, the only first-principles gyrokinetic simulation of an FRC in realistic geometry. Simulation in the scrape-off layer also represents the first inclusion of open field line geometry in the GTC formulation. Initial simulation parameters and results are presented. Pressure gradient driven driftwave modes are observed and effects of collisionality are considered. One notable caveat is that electromagnetic effects are expected to be important in high-β FRC plasmas, but are excluded in this study. Electromagnetic effects, already included in the GTC framework, will be investigated in FRCs in the future.

Interestingly, in the FRC core, ion scale instability is found to be suppressed, likely by large ion Larmour radius. Electron scale turbulence is also strongly stabilized, but details of possible electron scale modes are still under evaluation. In the scrape off layer, both ion and electron scale linear drift-waves are present and unstable. Remarkably, considering the electrostatic limitation of the computational model, linear instability thresholds in both the core and SOL have good qualitative agreement with experimental turbulence fluctuation measurements made with Doppler backscattering in the C-2 FRC experiment.[68] More detailed theoretical analysis of the physics in both the FRC core and SOL will be discussed in a forthcoming publication.[66] Comparisons against experimental data will be reevaluated as the computational model is refined.

The ultimate goal of first principles FRC simulations is to understand the transport scaling in the FRC plasma, towards the goal of creating a fusion reactor. Understanding the coupling between the core and SOL regions of the FRC is a critical piece of the transport scaling picture. Immediate efforts in the future are towards developing coupled core-SOL simulations. Other priorities include electromagnetic simulations and a Vlasov ion pusher, which has already been implemented in GTC, to accurately capture large ion Larmour radius effects.

[1]M. Tuszewski, "Field reversed configurations," Nucl. Fusion **28**(11), 2033 (1988).

[2]A. C. Kolb, C. B. Dobbie, and H. R. Griem, "Field mixing and associated neutron production in a plasma," Phys. Rev. Lett. **3**, 5–7 (1959).

[3]T. S. Green, "Evidence for the containment of a hot, dense plasma in a theta pinch," Phys. Rev. Lett. **5**, 297–300 (1960).

[4]Hiroyuki Maehara, Takuya Shibayama, Shota Notsu, Yuta Notsu, Takashi Nagao, Satoshi Kusaba, Satoshi Honda, Daisaku Nogami, and Kazunari Shibata, "Superflares on solar-type stars," Nature **485**, 478–481 (2012).

[5]S. A. Balbus and J. F. Hawley, "Instability, turbulence, and enhanced transport in accretion disks," Rev. Mod. Phys. **70**, 1–53 (1998).

[6]L. C. Steinhauer, "Review of field-reversed configurations," Phys. Plasmas 18(7), 070501 (2011).

[7]N. Rostoker, F. Wessel, H. Rahman, B. C. Maglich, B. Spivey, and A. Fisher, "Magnetic fusion with high energy self-colliding ion beams," Phys. Rev. Lett. 70, 1818–1821 (1993).

[8]M. W. Binderbauer and N. Rostoker, "Turbulent transport in magnetic confinement: How to avoid it," J. Plasma Phys. 56, 451–465 (1996).

[9]D. C. Barnes, J. L. Schwarzmeier, H. R. Lewis, and C. E. Seyler, "Kinetic tilting stability of field-reversed configurations," Phys. Fluids 29(8), 2616–2629 (1986).

[10]H. Naitou, T. Kamimura, and J. M. Dawson, "Kinetic effects on the convective plasma diffusion and the heat transport," J. Phys. Soc. Jpn. 46(1), 258–265 (1979).

[11]R. Horiuchi and T. Sato, "Full magnetohydrodynamic simulation of the tilting instability in a field-reversed configuration," Phys. Fluids B 1(3), 581–590 (1989).

[12]W. W. Heidbrink and G. J. Sadler, "The behaviour of fast ions in tokamak experiments," Nucl. Fusion 34(4), 535 (1994).

[13]M. W. Binderbauer, H. Y. Guo, M. Tuszewski, S. Putvinski, L. Sevier, D. Barnes, N. Rostoker, M. G. Anderson, R. Andow, L. Bonelli, F. Brandi, R. Brown, D. Q. Bui, V. Bystritskii, F. Ceccherini, R. Clary, A. H. Cheung, K. D. Conroy, B. H. Deng, S. A. Dettrick, J. D. Douglass, P. Feng, L. Galeotti, E. Garate, F. Giammanco, F. J. Glass, O. Gornostaeva, H. Gota, D. Gupta, S. Gupta, J. S. Kinley, K. Knapp, S. Korepanov, M. Hollins, I. Isakov, V. A. Jose, X. L. Li, Y. Luo, P. Marsili, R. Mendoza, R. Meekins, Y. Mok, A. Necas, E. Paganini, F. Pegoraro, R. Pousa-Hijos, S. Primavera, E. Ruskov, A. Qerushi, L. Schmitz, J. H. Schroeder, A. Sibley, A. Smirnov, Y. Song, X. Sun, M. C. Thompson, A. D. Van Drie, J. K. Walters, and M. D. Wyman, "Dynamic formation of a hot field reversed configuration with improved confinement by supersonic merging of two colliding high-β compact toroids," Phys. Rev. Lett. 105, 045003 (2010).

[14]M. Tuszewski, A. Smirnov, M. C. Thompson, T. Akhmetov, A. Ivanov, R. Voskoboynikov, D. C. Barnes, M. W. Binderbauer, R. Brown, D. Q. Bui et al., "A new high performance field reversed configuration operating regime in the C-2 device," Phys. Plasmas 19(5), 056108 (2012).

[15]H. Y. Guo, M. W. Binderbauer, T. Tajima, R. D. Milroy, L. C. Steinhauer, X. Yang, E. G. Garate, H. Gota, S. Korepanov, A. Necas, T. Roche, A. Smirnov, and E. Trask, "Achieving a long-lived high-beta plasma state by energetic beam injection," Nat. Commun. 6, 6897 (2015).

[16]M. W. Binderbauer, T. Tajima, L. C. Steinhauer, E. Garate, M. Tuszewski, L. Schmitz, H. Y. Guo, A. Smirnov, H. Gota, D. Barnes, B. H. Deng, M. C. Thompson, E. Trask, X. Yang, S. Putvinski, N. Rostoker, R. Andow, S. Aefsky, N. Bolte, D. Q. Bui, F. Ceccherini, R. Clary, A. H. Cheung, K. D. Conroy, S. A. Dettrick, J. D. Douglass, P. Feng, L. Galeotti, F. Giammanco, E. Granstedt, D. Gupta, S. Gupta, A. A. Ivanov, J. S. Kinley, K. Knapp, S. Korepanov, M. Hollins, R. Magee, R. Mendoza, Y. Mok, A. Necas, S. Primavera, M. Onofri, D. Osin, N. Rath, T. Roche, J. Romero, J. H. Schroeder, L. Sevier, A. Sibley, Y. Song, A. D. Van Drie, J. K. Walters, W. Waggoner, P. Yushmanov, K. Zhai, and TAE Team, "A high performance field-reversed configuration," Phys. Plasmas 22(5), 056110 (2015).

[17]S. Hamasaki and D. L. Book, "Numerical simulation of the anomalous transport process in radially compressed reversed-field configurations," Nucl. Fusion 20(3), 289 (1980).

[18]M. Tuszewski and R. K. Linford, "Particle transport in field-reversed configurations," Phys. Fluids 25(5), 765–774 (1982).

[19]A. L. Hoffman, R. D. Milroy, and L. C. Steinhauer, "Poloidal flux loss in a field-reversed theta pinch," Appl. Phys. Lett. 41, 31–33 (1982).

[20]A. W. Carlson, "A search for lower-hybrid-drift fluctuations in a field-reversed configuration using CO_2 heterodyne scattering," Phys. Fluids 30(5), 1497–1509 (1987).

[21]D. Winske and P. C. Liewer, "Particle simulation studies of the lower hybrid drift instability," Phys. Fluids 21(6), 1017–1025 (1978).

[22]J. U. Brackbill, D. W. Forslund, K. B. Quest, and D. Winske, "Nonlinear evolution of the lower-hybrid drift instability," Phys. Fluids 27(11), 2682–2693 (1984).

[23]N. T. Gladd, A. G. Sgro, and D. W. Hewett, "Microstability properties of the sheath region of a field-reversed configuration," Phys. Fluids 28(7), 2222–2234 (1985).

[24]N. T. Gladd, J. F. Drake, C. L. Chang, and C. S. Liu, "Electron temperature gradient driven microtearing mode," Phys. Fluids 23(6), 1182–1192 (1980).

[25]R. Farengo, P. N. Guzdar, and Y. C. Lee, "Collisionless electron temperature gradient driven instability in field reversed configurations," Phys. Fluids B 1(11), 2181–2185 (1989).

[26]N. A. Krall, "Low-frequency stability for field reversed configuration parameters," Phys. Fluids 30(3), 878–883 (1987).

[27]D. E. Hastings and J. E. McCune, "The high universal drift mode," Phys. Fluids 25(3), 509–517 (1982).

[28]R. K. Linford, in Unconventional Approaches to Fusion, edited by B. Brunelli and G. G. Leotta (Plenum Press, New York and London, 1982), Vol. 13, p. 463.

[29]A. L. Hoffman and R. D. Milroy, "Particle lifetime scaling in field-reversed configurations based on lower-hybrid-drift resistivity," Phys. Fluids 26(11), 3170–3172 (1983).

[30]S. P. Auerbach and W. C. Condit, "Classical diffusion in a field-reversed mirror," Nucl. Fusion 21(8), 927 (1981).

[31]K. Nguyen and T. Kammash, "Classical transport coefficients in a field-reversed configuration," Plasma Phys. 24(2), 177 (1982).

[32]R. A. Clemente and C. E. Grillo, "Internal tilting and classical transport for field-reversed configurations based on the Maschke-Hernegger solution," Phys. Fluids 27(3), 658–660 (1984).

[33]R. A. Clemente and E. M. Freire, "Classical particle-diffusion time for analytical compact tori equilibria," Plasma Phys. Controlled Fusion 28(7), 951 (1986).

[34]Y. Aso, S. Himeno, and K. Hirano, "Experimental studies on energy transport in a reversed-field theta pinch," Nucl. Fusion 23(6), 751 (1983).

[35]D. J. Rej and M. Tuszewski, "A zero-dimensional transport model for field-reversed configurations," Phys. Fluids 27(6), 1514–1520 (1984).

[36]S. Hamada, "A model of equilibrium transport and evolution of field reversed configurations," Nucl. Fusion 26(6), 729 (1986).

[37]D. C. Quimby, A. L. Hoffman, and G. C. Vlases, "Linus cycle calculations including plasma transport and resistive flux loss," Nucl. Fusion 21(5), 553 (1981).

[38]E. J. Caramana, "The long-time evolution approximation for a quasi-one-dimensional plasma system," Phys. Fluids 28(12), 3557–3566 (1985).

[39]K. A. Werley, "One-and-a-quarter-dimensional transport modeling of the field-reversed configuration," Phys. Fluids 30(7), 2129–2138 (1987).

[40]D. E. Shumaker, "Transport simulation of a field-reversed configuration plasma," Fusion Science and Technology 13(4), 555–576 (1988).

[41]I. Holod, W. L. Zhang, Y. Xiao, and Z. Lin, "Electromagnetic formulation of global gyrokinetic particle simulation in toroidal geometry," Phys. Plasmas 16(12), 122307 (2009).

[42]Z. Lin, T. S. Hahm, W. W. Lee, W. M. Tang, and R. B. White, "Turbulent transport reduction by zonal flows: Massively parallel simulations," Science 281, 1835 (1998).

[43]Y. Xiao and Z. Lin, "Turbulent transport of trapped-electron modes in collisionless plasmas," Phys. Rev. Lett. 103(8), 085004 (2009).

[44]W. Zhang, Z. Lin, and L. Chen, "Transport of energetic particles by microturbulence in magnetized plasmas," Phys. Rev. Lett. 101(9), 095001 (2008).

[45]H. S. Zhang, Z. Lin, and I. Holod, "Nonlinear frequency oscillation of Alfvén eigenmodes in fusion plasmas," Phys. Rev. Lett. 109(2), 025001 (2012).

[46]Z. Wang, Z. Lin, I. Holod, W. W. Heidbrink, B. Tobias, M. Van Zeeland, and M. E. Austin, "Radial localization of toroidicity-induced Alfvén eigenmodes," Phys. Rev. Lett. 111(14), 145003 (2013).

[47]J. McClenaghan, Z. Lin, I. Holod, W. Deng, and Z. Wang, "Verification of gyrokinetic particle simulation of current-driven instability in fusion plasmas. I. Internal kink mode," Phys. Plasmas 21(12), 122519 (2014).

[48]D. Liu, W. Zhang, J. McClenaghan, J. Wang, and Z. Lin, "Verification of gyrokinetic particle simulation of current-driven instability in fusion plasmas. II. Resistive tearing mode," Phys. Plasmas 21(12), 122520 (2014).

[49]R. B. White, The Theory of Toroidally Confined Plasmas, 3rd ed. (Imperial College Press, London, 2014).

[50]W. D. D'haeseleer, W. N. G. Hitchon, J. L. Shohet, J. D. Callen, and D. W. Kerst, Flux Coordinates and Magnetic Field Structure. A Guide to a Fundamental Tool of Plasma Theory (Springer-Verlag, Berlin Heidelberg, 1991).

[51]A. Yu. Chirkov and V. I. Khvesyuk, "Electromagnetic drift instabilities in high-plasma under conditions of a field reversed configuration," Phys. Plasmas 17(1), 012105 (2010).

[52]I. Holod and Z. Lin, "Verification of electromagnetic fluid-kinetic hybrid electron model in global gyrokinetic particle simulation," Phys. Plasmas 20(3), 032309 (2013).

[53]I. Holod, D. P. Fulton, and Z. Lin, "Microturbulence in DIII-D tokamak pedestal. II. Electromagnetic instabilities," Nucl. Fusion 55(9), 093020 (2015).

[54] J. Bao, Z. Lin, A. Kuley, and Z. X. Wang, "Electromagnetic particle simulation model for nonlinear processes of lower hybrid waves in fusion plasmas," (unpublished).

[55] M. Okamoto, T. Tajima, N. Rostoker, B. Coppi, A. Ishida, and Y. Nakamura, "Summary," AIP Conf. Proc. **311**(1), 325–326 (1994).

[56] A. H. Boozer, "Plasma equilibrium with rational magnetic surfaces," Phys. Fluids **24**(11), 1999–2003 (1981).

[57] L. Galeotti, D. C. Barnes, F. Ceccherini, and F. Pegoraro, "Plasma equilibria with multiple ion species: Equations and algorithm," Phys. Plasmas **18**(8), 082509 (2011).

[58] W. W. Lee, "Gyrokinetic approach in particle simulation," Phys. Fluids **26**(2), 556–562 (1983).

[59] T. Tajima, *Computational Plasma Physics—With Applications to Fusion and Astrophysics*, Benjamin Frontier Series (Addison-Wesley, Reading, MA, 1989).

[60] A. M. Dimits and W. W. Lee, "Partially linearized algorithms in gyrokinetic particle simulation," J. Comput. Phys. **107**(2), 309–323 (1993).

[61] S. E. Parker and W. W. Lee, "A fully nonlinear characteristic method for gyrokinetic simulation," Phys. Fluids B **5**(1), 77–86 (1993).

[62] J. K. Koga and T. Tajima, "The δf algorithm for beam dynamics," J. Comput. Phys. **116**(2), 314–329 (1995).

[63] Y. Xiao, I. Holod, Z. X. Wang, Z. Lin, and T. Zhang, "Gyrokinetic particle simulation of microturbulence for general magnetic geometry and experimental profiles," Phys. Plasmas **22**(2), 022516 (2015).

[64] W. W. Lee, "Gyrokinetic particle simulation model," J. Comput. Phys. **72**(1), 243–269 (1987).

[65] S. Balay, S. Abhyankar, M. F. Adams, J. Brown, P. Brune, K. Buschelman, L. Dalcin, V. Eijkhout, W. D. Gropp, D. Kaushik, M. G. Knepley, L. Curfman McInnes, K. Rupp, B. F. Smith, S. Zampini, and H. Zhang, Portable, Extensible Toolkit for Scientific Computation, PETSC, 2014, http://www.mcs.anl.gov/petsc.

[66] C. K. Lau, D. P. Fulton, I. Holod, Z. Lin, L. Schmitz, T. Tajima, and M. W. Binderbauer, "Electrostatic Drift-wave Instability in Field-Reversed Configuration," (unpublished).

[67] Z. Lin, W. M. Tang, and W. W. Lee, "Gyrokinetic particle simulation of neoclassical transport," Phys. Plasmas **2**(8), 2975–2988 (1995).

[68] L. Schmitz, D. Fulton, E. Ruskov, C. Lau, B. H. Deng, T. Tajima, M. W. Binderbauer, I. Holod, Z. Lin, H. Gota, M. Tuszewski, S. A. Dettrick, L. C. Steinhauer, D. Gupta, W. A. Peebles, T. Akhmetov, J. Douglass, E. Garate, A. Ivanov, S. Korepanov, A. Smirnov, M. C. Thompson, E. Trask, and the TAE Team, "First evidence of suppressed ion-scale turbulence in a hot high-β plasma," Nat. Commun. (submitted).